Received: 29 August 2023 | Revised: 6 December 2023 | Accepted: 9 December 2023

DOI: 10.1111/ejn.16239

SPECIAL ISSUE ARTICLE

EJN European Journal of Neuroscience FENS WILEY

Different electrophysiological profiles of genetically labelled dopaminergic neurons in the mouse midbrain and olfactory bulb

Maggy Yu Hei Lau | **Sana Gadiwalla** | **Susan Jones** | **Elisa Galliano**

Department of Physiology, Development and Neuroscience, University of Cambridge, UK

Correspondence
Susan Jones and Elisa Galliano, Department of Physiology, Development and Neuroscience, University of Cambridge, UK.
Email: sj251@cam.ac.uk and eg542@cam.ac.uk

Present address
Sana Gadiwalla, Faculty of Medicine, School of Health Sciences, University of Iceland, Reykjavik, Iceland.

Funding information
Royal Society Research, Grant/Award Number: RGS\R1\19148; URKI Biotechnology and Biological Sciences Research Council (BBSRC), Grant/Award Number: BB\W014688\1; Newton Trust ISSF Grant

Edited by: Louis-Eric Trudeau

Abstract

Dopaminergic (DA) neurons play pivotal roles in diverse brain functions, spanning movement, reward processing and sensory perception. DA neurons are most abundant in the midbrain (Substantia Nigra pars compacta [SNC] and Ventral Tegmental Area [VTA]) and the olfactory bulb (OB) in the forebrain. Interestingly, a subtype of OB DA neurons is capable of regenerating throughout life, while a second class is exclusively born during embryonic development. Compelling evidence in SNC and VTA also indicates substantial heterogeneity in terms of morphology, connectivity and function. To further investigate this heterogeneity and directly compare form and function of midbrain and forebrain bulbar DA neurons, we performed immunohistochemistry and whole-cell patch-clamp recordings in ex vivo brain slices from juvenile DAT-tdTomato mice. After confirming the penetrance and specificity of the dopamine transporter (DAT) Cre line, we compared soma shape, passive membrane properties, voltage sags and action potential (AP) firing across midbrain and forebrain bulbar DA subtypes. We found that each DA subgroup within midbrain and OB was highly heterogeneous, and that DA neurons across the two brain areas are also substantially different. These findings complement previous work in rats as well as gene expression and in vivo datasets, further questioning the existence of a single "dopaminergic" neuronal phenotype.

KEYWORDS
dopamine, immunohistochemistry, midbrain, olfactory bulb, patch clamping (electrophysiology)

Abbreviations: AP, action potential; CV, coefficient of variation; DA, dopaminergic; DAT, dopamine transporter; I-O, input–output; ISI, inter-spike interval; MT, medial terminal nucleus of the accessory optic tract; OB, olfactory bulb; OR, onset rapidness; PBS, phosphate buffered saline; PC, principal components; PCA, principal components analysis; PFA, paraformaldehyde; Rm, resting membrane potential; ROI, region of interest; SNC, substantia nigra pars compacts; tdT, tandem dimer Tomato; TH, tyrosine hydroxylase; VTA, ventral tegmental area.

1 | INTRODUCTION

The neurotransmitter dopamine (DA) is instrumental in modulating wide-ranging functions, which include motor control, learning and emotional regulation (Berke, 2018). Given such broad behavioural reach, it is somewhat surprising that in the mammalian brain, DA is only produced by a few clusters of cells, which together account for less than 1% of the total neuron number (Chinta & Andersen, 2005). Almost all dopaminergic neurons are localised to the midbrain cell groups A8 (retrorubal), A9 (substantia nigra pars compacta [SNC]) and A10 (ventral tegmental area [VTA]) (Björklund & Dunnett, 2007; Dahlstroem & Fuxe, 1964; Garritsen et al., 2023). These midbrain DA neurons have distinct inputs, axonal projections, functional roles and clinical relevance (Ungless & Grace, 2012). Malfunctioning, mis-development or degeneration of these neurons results in pathologies such as Parkinson's disease (PD) (Poewe et al., 2017; Sillitoe & Vogel, 2008) while substance abuse disorders at least initially involve VTA projections to the ventral striatum (Lüscher et al., 2020). Thus, unsurprisingly, the physiology and pathology of midbrain DA neurons have long been the focus of intense fundamental and translational research (Bissonette & Roesch, 2016). Outside the midbrain resides the less investigated minority (≈10%) of DA groups. These are found in the retina, diencephalon (hypothalamic groups A11–15) and in the forebrain where group A16 in the olfactory bulb (OB) is the most abundant (Andén et al., 1965; Björklund & Dunnett, 2007; Halász et al., 1981). OB DA neurons are local inhibitory interneurons, which, by co-releasing DA and GABA in the bulbar glomerular layer, modulate the information transfer at the first synapse in the olfactory pathway and contribute to shape olfactory behaviour (Banerjee et al., 2015; Economo et al., 2016; Hsia et al., 1999; McGann, 2013; Pignatelli et al., 2005). Interestingly, most OB DA neurons can regenerate throughout the animal's lifetime (Bonzano et al., 2016). Indeed, an increase in their number, rather than the degeneration occurring in the midbrain, has been reported in patients with PD, and given their inhibitory role it could account for the hyposmia/anosmia associated with the disease (Huisman et al., 2004).

Within each anatomically defined group, DA neurons have historically been considered homogeneous populations of cells, which express tyrosine hydroxylase (TH, the rate limiting enzyme in the catecholamine synthesis (White & Thomas, 2012)). There is now compelling evidence for functional heterogeneity ((Chiodo et al., 1984; Greene, 2006; Margolis et al., 2006; Neuhoff et al., 2002; Poulin et al., 2018; Tiklová et al., 2019); reviewed by (Morales & Margolis, 2017; Poulin et al., 2020; Roeper, 2013)). A potential caveat is that DA neuron identification often relies on physiological methods (Ungless & Grace, 2012) — for example, in brain slices, the action potential (AP) waveform or the spontaneous firing rate in current clamp recordings, or the presence of a hyperpolarisation-activated cation current, Ih, in voltage clamp recordings. These criteria might be viewed as indirect and might not reflect the full heterogeneity of DA neurons (Margolis et al., 2006; Neuhoff et al., 2002). The emergence of technologies allowing the generation of mouse lines which target specific cell types confirmed that DA neurons within the OB are highly heterogeneous in terms of their developmental profile, morphology and electrophysiological properties (Chand et al., 2015; Galliano et al., 2018; Kosaka et al., 2020). Somewhat surprisingly, no study has yet compared the functional heterogeneity of genetically identified DA neuron electrophysiological properties within VTA, and across the midbrain.

To date, OB DA neurons show perhaps the highest level of morphological and functional heterogeneity and can be cleanly divided into two subgroups. While the smallest subgroup consists of neurons with far-branching dendrites and an axon, and which are born exclusively during early embryonic development ('standard' neurons, sometimes called short-axon cells), the majority of OB DA cells do not have an axon but release GABA and dopamine from narrowly branched dendrites, and undergo life-long neurogenesis (Bonzano et al., 2016; Chand et al., 2015; Galliano et al., 2018; Kiyokage et al., 2010; Kosaka et al., 2020; Tufo et al., 2022). The neurogenic properties of OB DA neurons and their ability to insert themselves into a pre-existing circuit have prompted their exploration as potential candidates for adult stem cell replacement strategies in models of degeneration of midbrain DA neurons (Cave et al., 2014; Deleidi et al., 2011). However, given the recent confirmation that only the anaxonic OB DA subtype can undergo adult neurogenesis, it is important to clarify whether they share any functional properties with the neurons that they could potentially replace.

In this study, we took advantage of the DAT-Cre transgenic mouse line to insert a fluorescent tag in neurons expressing the dopamine transporter (DAT) promotor (Bäckman et al., 2006). In thus-identified DA neurons, we investigated their morphological and functional heterogeneity within and between midbrain and OB. Overall, we aimed to answer this question: do all DA neurons share common neurophysiological features?

2 | METHODS

2.1 | Animals

DAT-Cre (B6.SJL-Slc6a3 tm1.1(cre)Bkmn/J, Jax stock 006660) mice were crossed with flox-tdTomato (B6;129S6-Gt (ROSA)26Sortm9(CAG-tdTomato)Hze/J, Jax

stock 007909). Transgenic DAT-Cre × flex-tdTomato (tdT) mice of either gender were used aged postnatal day 16–36 in all experiments in accordance with the Animals (Scientific procedures) Act 1986 and with AWERB (Animal Welfare and Ethical Review Board) approval. Mice were housed in 12-hour light–dark cycle in an environmentally controlled room with ad libitum access to water and food.

2.2 | Immunohistochemistry

Mice were anesthetised with an overdose of pentobarbital and then perfused with 20 ml PBS with heparin (20 units·ml^{-1}), followed by 20 ml of 1% paraformaldehyde (PFA; TAAB Laboratories; in 3% sucrose, 60 mM PIPES, 25 mM HEPES, 5 mM EGTA, and 1 mM $MgCl_2$). The brains were dissected and post-fixed in 1% PFA for 2–7 days, then embedded in 5% agarose and sliced horizontally at 50 μm using a vibratome (VT1000S, Leica). Free-floating slices containing SNC, VTA and OB were washed with PBS and incubated in 5% normal goat serum (NGS) in PBS/Triton/azide (0.25% triton, 0.02% azide) for 2 h at room temperature. They were then incubated in primary antibody (TH, mouse, Millipore MAB318, 1:500; Ds-Red, rabbit, Clontech 632,496, 1:500,) diluted in a PBS/Triton/azide for 2 days at 4°C. Slices were then washed three times for 5 min with PBS, before being incubated in secondary antibody solution (mouse 488 and rabbit 633 Alexa Fluor®; 1:1000 in PBS/Triton/azide) for 3 h at room temperature. After washing in PBS, slices underwent an additional counterstaining step with 0.2% Sudan black in 70% ethanol at room temperature for 3 min to minimise autofluorescence, and then they were mounted on glass slides (Menzel-Gläser) with FluorSave. Unless stated otherwise all reagents were purchased from Sigma.

2.3 | Fixed-tissue imaging and analysis

All images were acquired with a laser scanning confocal microscope (Zeiss LSM 710) using appropriate excitation and emission filters, a pinhole of 1 airy unit and a 40× oil immersion objective. Laser power and gain were set for each image and in each channel to prevent signal saturation while permitting clear delineation of neuronal somas for quantification. All quantitative analysis was performed with Fiji (Image J). Images were taken with a 0.7× zoom (0.593 μm/pixel), 512 × 512 pixels, and in z-stacks with 1 μm steps across the entire depth of the slice. In all animals, images were sampled from three slices taken from the upper, middle and lower third of the portion of the brain in the dorsal–ventral axis containing the midbrain. SNC was defined as being adjacent (anteriorly and posteriorly) to the medial terminal nucleus of the accessory optic tract (MT); VTA was defined as being between MT and the midline. The OB was sampled both rostrally and caudally. To avoid selection biases, all cells present in the stack and positive for either identifying marker (TH or DsRed) were measured. DsRed immunofluorescence in the 633 channel was analysed instead of the genetically encoded tdT fluorescence in the 580 channel to standardise comparison with the TH immunofluorescence and account for antibody penetration. TH and/or DsRed positive OB DA cells were included in the analysis only if their soma was in or bordering with the glomerular layer. For both the TH and DsRed channels, the staining intensity of each ROI (expressed as mean grey value) was compared with the background staining in each image, defined by manually drawing a 'background region of interest (ROI)' in an area clearly devoid of cells. A cell was considered TH- or DsRed-positive if its mean grey value in the respective channels was bigger than 1.2 times the background ROI value.

Soma area was measured at the single plane including the cell's maximum diameter by drawing a ROI with the free-hand drawing tool. To validate the manual analysis, a subset of images across the three brain areas was measured by the same experimenter twice (with over 1.5 years inter-measurement interval, blind) and by two independent experimenters (all p values >0.17). Fiji (ImageJ) shape descriptors analysis was used on these ROIs to extract maximum diameter (Feret's diameter, the longest distance between any two points along the selection boundary), and roundness ($4*area/(\pi*major\_axis^2)$, the inverse of the aspect ratio). DA cell density was calculated for each image by dividing the number of analysed DsRed-positive cells by the volume of the SNC/VTA/glomerular layer (z depth × ROI area, drawn and measured in a maximum intensity projection of the DsRed channel).

2.4 | Electrophysiology

Mice were anesthetised with isoflurane and then decapitated. The desired brain area (either midbrain or OB) was then dissected and submerged in ice-cold sucrose solution containing (in mM): 240 sucrose, 5 KCl, 1.25 Na_2HPO_4, 2 $MgSO_4$, 1 $CaCl_2$, 26 $NaHCO_3$ and 10 D-Glucose continuously bubbled with 95% O_2 and 5% CO_2. Horizontal slices of the midbrain (200–250 μm) and OB (300 μm) were made using a Campden Instruments 7000 Vibroslicer. Slices were then transferred to a submersion incubation chamber with a glucose artificial cerebrospinal fluid

(ACSF) solution containing (in mM): 124 NaCl, 5 KCl, 1.25 Na_2HPO_4, 5 $MgSO_4$, 2 $CaCl_2$, 26 $NaHCO_3$ and 20 D-Glucose, maintained at 30°C in 95% O_2 and 5% CO_2 for 30 min to 5 h before patch clamp recordings.

Patch pipettes were made from borosilicate glass (PG150T-7.5, Harvard Apparatus Ltd., Kent, UK) to achieve a tip resistance of 1.5–5.0 MΩ (larger tips for midbrain, smaller for OB) when filled with solution containing (in mM): 124 K-Gluconate, 9 KCl, 10 KOH, 4 NaCl, 10 HEPES, 28.5 Sucrose, 4 Na2ATP, 0.3 Na3GTP (pH 7.20–7.30; 270–300 mOsm). DA cells were visualised using an upright microscope (Olympus BX51WI) equipped with a 4× air objective and a 40× water immersion objective, and SciCam camera (Scientifica). tdT fluorescence was revealed by LED (CoolLED pE-100) excitation. Under low power magnification, the glomerular layers in OB slices were visually located as circular structures proximal to the olfactory sensory nerves. The SNC and VTA in the midbrain slices were located by visually locating the medial terminal nucleus of the accessory optic tract. The SNC was identified as the region of DA neurons adjacent to MT and the VTA was identified as the region of DA neurons medial to the MT. During recordings, slices were perfused with ACSF at 30 ± 2°C with an inline and chamber heater (Warner Instrument Corporation, MA, USA). Whole-cell patch clamp recordings were performed using an Axon Axopatch 200B patch clamp amplifier (Molecular Devices, CA, USA). Signals were filtered at 2 kHz then acquired and digitised at 20 kHz using a Micro 1401 acquisition unit (Cambridge Electronic Design, Cambridge, UK). DA neurons were voltage clamped to −60 mV and their passive properties were probed between each experimental protocol with test pulses of 5 mV for 10 ms. Recordings were excluded if the series resistance (Rs) exceeded 20 MΩ (for midbrain neurons) or 30 MΩ (for OB neurons); or input resistance (Ri) was lower than 100 MΩ (both midbrain and OB neurons). Recordings were also excluded when two test pulses measured before and after the recording varied by over 20%. Experimental recordings were acquired and analysed using Spike 2 (Version 4; Cambridge Electronic Design, Cambridge, UK).

Single AP experiments were performed in current clamp in continuous mode. DA neurons were clamped to −60 ± 3 mV and 12 pulses of 10 ms current of increasing amplitudes were injected at 3 s intervals into midbrain DA neurons in 40pA increments (0–480pA) and into OB DA neurons in 10pA increments (0–120pA). Single AP experiments were only analysed in Spike2 if (a) they were the first AP fired in the 12-sweep 10-ms experiment; (b) the membrane potential before spiking was at −60 ± 3 mV; (c) the AP peak overshot 0 mV. Current threshold was defined as the current needed to elicit the first AP. Voltage threshold was measured at the potential at which dV/dt first passed 10 V/s. AP properties were measured as follows: AP peak at the highest voltage an AP reaches; AP after-hyperpolarisation (AHP) at the lowest voltage an AP reaches in the AHP overshoot phase after spiking; AP amplitude as the voltage difference between the voltage threshold and the AP peak of spike; AP width at half height where the AP half height is measured at the halfway point between the voltage threshold and the peak of spike.

For OB DA neurons, the classification between biphasic/putative axon-bearing (OBb) and monophasic/putative anaxonic (OBm) DA neurons was performed based on the onset rapidness (OR) of their APs and visually confirmed by ML and EG. For each OB DA neuron, the first AP from their single spike experiments were extracted from Spike 2 and converted into .abf format via ABF Utility 2 (Synaptosoft Inc., NJ, USA). The truncated AP was analysed by custom-written routines in MATLAB written by Matthew Grubb (Galliano et al., 2019). Voltage threshold for the analysis of onset rapidness was taken from the MATLAB algorithm as when the rate of change of membrane potential over time (dV/dt) passed 10 V/s. The onset rapidness of an AP was measured from the slope of a linear fit to the phase plane plot at voltage threshold. In line with our previous findings (Chand et al., 2015; Galliano et al., 2018, 2021) DA neurons with an OR ≥5 ms^{-1} were classified as biphasic/putative axon-bearing, DA neurons with an OR <4 ms^{-1} were classified as monophasic/putative anaxonic. DA neurons with an 5 < OR<4 ms^{-1} are not cleanly classifiable, and were thus discarded.

For repetitive firing experiments, 500 ms pulses of current of increasing amplitudes were injected at 5 s intervals from 0–480pA at 40pA increments for midbrain DA neurons, and from 0–120pA at 10pA intervals for OB DA neurons. APs recorded from the multiple AP experiments were only analysed if their membrane potential before spiking was at −60 ± 3 mV and the peak of AP overshot 0 mV. Input–output (I-O) firing plots were generated by plotting the number or frequency of APs against the amount of current injected in each sweep. The slope of the I-O curve measured between the sweep with a non-zero AP and the first sweep where the maximum number of APs fired throughout the experiment was recorded. The following parameters were measured only from the sweep where the maximum number of APs were fired: first AP delay, measured by the time interval between the start of current injection (identified as when a noticeable membrane depolarisation is observed) and the peak of the first AP; time between the first and last AP; average interspike interval (ms); AP frequency, measured by number of APs/time between the first and last AP * 1000.

To investigate sag potentials, 3 s current injections of increasingly hyperpolarising steps in −20pA increments

were applied in current-clamp mode until the point where the initial voltage response (V_P) passed −100 mV. V_P was the minimum voltage response within the first 100 ms of the current step. To quantitatively compare sag potentials, we calculated the sag amplitude as the difference between the lowest voltage reached (V_P, peak) and the steady-state (V_{SS}, average voltage 100 ms before the end of the hyperpolarisation step), and the sag index (Angelo et al., 2012) using the equation [sag index = $(V_H - V_{SS}) / (V_H - V_P)$], where V_H was defined as the average voltage 500 ms before the current injection.

2.5 | Statistical analysis and data availability

Statistical analysis was carried out using Prism (GraphPad). 'N' refers to number of animals and 'n' indicates number of cells. Sample distributions were assessed for normality with the D'Agostino and Pearson omnibus test, and parametric or non-parametric tests carried out accordingly. α values were set to ≤0.05, and all comparisons were two-tailed. For multilevel analyses, cells were nested on animals or brain areas (Aarts et al., 2014). Repetitive firing I-O curves were fitted by a mixed model with Geisser–Greenhouse correction, and Benjamini, Krieger and Yekutieli two-stage step-up method to control for false discovery rate. Principal component analysis (PCA) on electrophysiological data was performed on data standardised to have a mean of 0 and a standard deviation of 1. Principal components (PCs) were selected based on the Kaiser rule, where PCs were selected only if they had an eigenvalue greater than one. This selection was also evaluated with a scree plot. All PCAs were unsupervised; each cell was later coloured on the plot, allowing us to visually assess functionally significant clustering. Loading scores were calculated based on standardised data and calculated using the following formula: (Eigenvector * sqrt [Eigenvalue]). The full dataset can be found on the University of Cambridge Apollo repository (doi.org/10.17863/CAM.102763) under a CC-BY license.

3 | RESULTS

3.1 | DAT-TH colocalisation rates and morphological differences between and within midbrain and forebrain OB DA neurons

When crossed with floxed fluorescent reporter lines, the transgenic mouse line DAT-Cre (Bäckman et al., 2006) allows for live visualisation of DA cells expressing the DAT. To assess the veracity and penetrance of DAT-tdT labelling across the dorso-ventral axis in midbrain and OB (Lammel et al., 2015; Papathanou et al., 2019; Stuber et al., 2015), we performed immunohistochemistry in fixed horizontal brain slices from juvenile animals. To enhance the genetic tomato label, we used an anti-DsRed antibody and co-stained the brain slices sampled at different dorso-ventral planes with antibodies against TH, the rate-limiting enzyme in the biosynthesis of catecholamines (Figure 1A–B). In the SNC, the vast majority of cells positive for DsRed were also stained by TH, indicating excellent overlap of DAT and TH expression (double positive 99.34 ± 0.6%, $DsRed^+/TH^-$ 0.44 ± 0.44%, $DsRed^-/TH^+$ 0.22 ± 0.22%, n = 658, N = 4; Figure 1C), a pattern of penetrance consistently high across the dorsoventral axis (Figure 1D; χ^2 test, $p = 0.95$). In the VTA, the expression patterns were more heterogeneous overall (double positive 85.40 ± 5.32%%, $DsRed^+/TH^-$ 8.75 ± 4.43%, $DsRed^-/TH^+$ 6.00 ± 2.35%, n = 752, N = 4; Figure 1C), and the colocalisation in dorsal slices was particularly variable (Figure 1D, χ^2 test, $p = 0.02$). In the OB, in line with previous reports (Byrne et al., 2022; Galliano et al., 2018), only around 70% of cells expressed both the genetically encoded DAT-tomato label and TH (double positive 72.17 ± 3.39%, $DsRed^+/TH^-$ 11.7 ± 1.50%, $DsRed^-/TH^+$ 16.05 ± 2.35%, n = 2652, N = 4; Figure 1C). The penetrance of the genetic label was equally incomplete across the dorso-ventral axis (Figure 1D, χ^2 test, $p = 0.77$) and the rostro-caudal axis (χ^2 test, $p = 0.91$). To match the subsequent electrophysiological experiments where only DAT-positive cells were recorded in acute brain slices, the few $DsRed^-/TH^+$ cells imaged in the fixed-tissue configuration were removed from further morphological analysis. The soma area of DAT-tdT positive neurons varied considerably within the midbrain (Figure 1E, Table 1, nested *t*-test, $p = 0.03$), and between midbrain and forebrain OB (Figure 1E, Table 1, nested *t*-test, $p < 0.001$), with SNC neurons being 40% larger than VTA cells and almost triple the size of OB neurons. All three soma area distributions were not Gaussian with positive values for both skewness and kurtosis, but the OB distribution was particularly asymmetrical. Consistent with previous work (Galliano et al., 2018; Pignatelli et al., 2005), the OB soma size distribution peaked around 70 μm^2 (putative anaxonic neurons capable of regenerating throughout the animal's lifetime) and a long tail of less numerous cells with areas overshooting 100 μm^2 (putative axon-bearing neurons born exclusively during early embryonic development). Across all brain areas, the DAT-tdT neurons' maximum soma diameter strongly correlated with its area (Figure 1F, Table 1). Moreover, OB DAT-tdT cells were rounder than in midbrain as well as smaller, while SNC

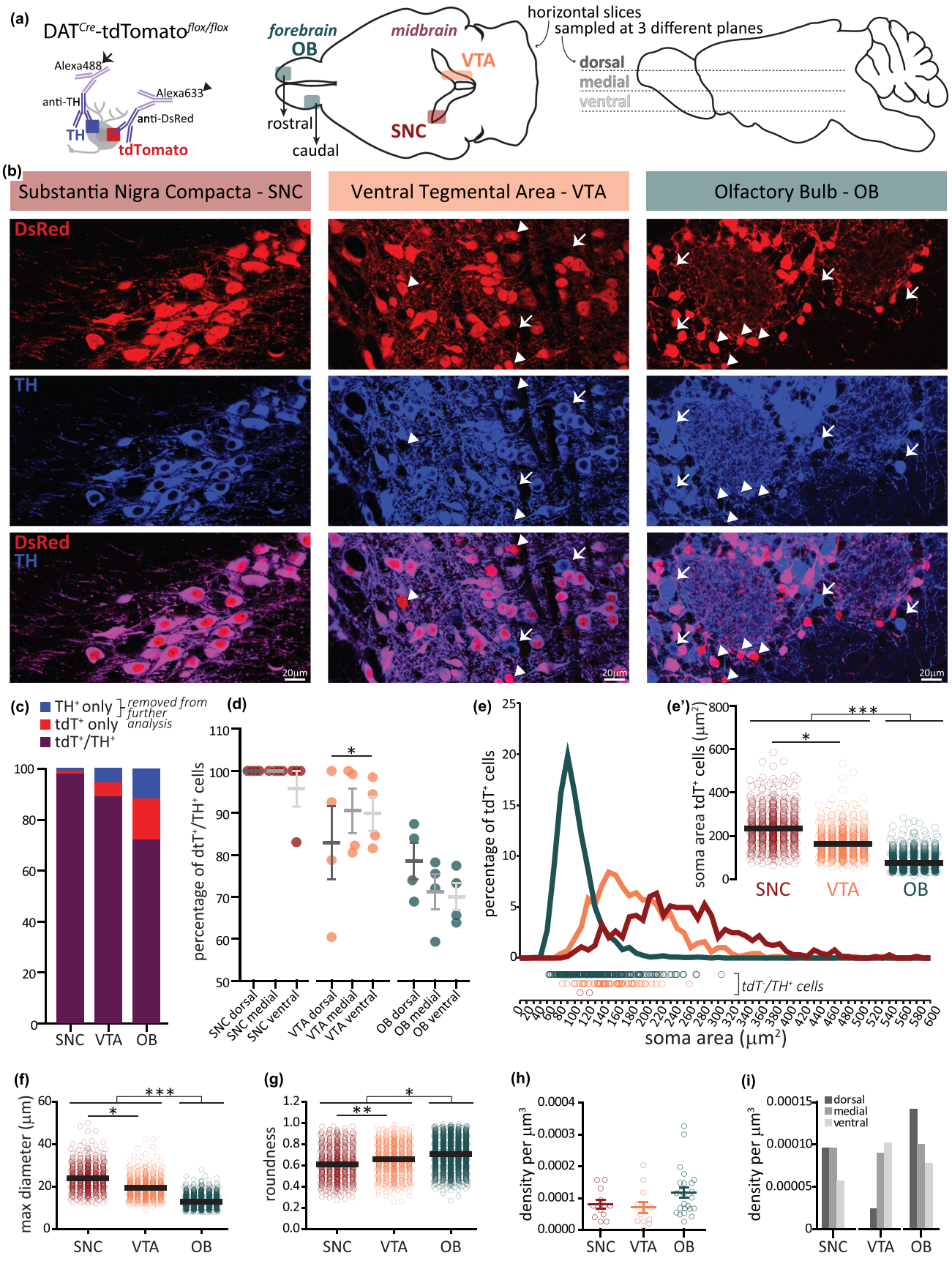

FIGURE 1 Legend on next page.

FIGURE 1 Genetic label penetrance and neuronal morphology differences in forebrain OB and midbrain. (a) Left: schematic representation of the immunolabelling strategy for tyrosine hydroxylase (TH) and DAT-tdTomato expression enhanced with anti-DsRed antibodies. Centre: location of forebrain olfactory bulb (OB) and midbrain substantial nigra compacta (SNC) and ventral tegmental area (VTA) DA neurons in the horizontal plane. Right: horizontal slices sampling across the dorso-ventral axis; the OB was additionally sampled across the rostro-caudal axis as indicated in the central schematic. (b) Example labelling of DsRed-enhanced tdTomato (red) and TH (blue) in SNC (left), VTA (centre) and OB (right). Triangles indicate cells positive for DsRed and negative for TH, and vice versa arrows indicate cells negative for DsRed and positive for TH. (c) Percentage of all cells labelled that were positive for both DsRed and TH (purple), DsRed only (red) or TH only (blue), in SNC (n = 658, N = 4), VTA (n = 752, N = 4) and OB (n = 2652, N = 4). (d) Percentage of cells positive for both DsRed and TH in dorsal, medial and ventral slices in the three brain areas. (e) DAT-tdTomato positive cells (DsRed+/TH + and DsRed +/TH-) soma area distribution in SNC (red), VTA (orange) and OB (green); circles above x-axis indicate the area of individual DsRed+/TH- neurons. Inset in E': individual soma area values and median for SNC (n = 656, N = 4), VTA (n = 688, N = 4), and OB (n = 2337, N = 4). (f) Maximum somatic diameter and (g) soma roundness of DAT-tdTomato positive neurons. (H) Density of DAT-tdTomato positive neurons per μm^3 in each brain region and (i) in the dorsal, medial or ventral tier of each region. Circles are individual data points, thick lines are mean values, $*p < 0.05$; $**p < 0.01$, $*p < 0.001$; for further quantification see Table 1.

neurons were the largest and least round (Figure 1G, Table 1). Finally, we found that despite the soma size differences, the DAT-tdT neuron density was similar between forebrain OB and midbrain (Figure 1H, Table 1, nested t-test, $p = 0.19$), and within each brain area along the dorso-ventral axis — although density within the VTA was rather heterogeneous (Figure 1I).

3.2 | Passive electrical properties differ between the forebrain OB and midbrain populations of DA neurons

To investigate the functional similarities/differences between and within forebrain OB and midbrain DA neurons, we switched to an acute slice configuration and performed whole-cell patch-clamp recordings in DAT-tdT neurons. Given that neuronal excitability is partially determined by the passive electrical properties of the plasma membrane, we compared the neurons' passive properties in response to a subthreshold voltage step (5 mV for 10 ms; Figure 2A). The resting membrane potential (Rm) was not different between midbrain and OB DA neurons overall, nor between the midbrain subpopulations in SNC and VTA (Figure 2B, Table 2). As reported previously (Galliano et al., 2018, 2021), with whole-cell patch clamp it is possible to further classify DA subtypes in the OB. Specifically, anaxonic versus axon-bearing OB DA subtypes can be teased apart on the basis of their AP planar phase plot and onset rapidness (see Methods for details). In line with previous work, we found that Rm was significantly more hyperpolarised in putative axon-bearing DA cells (OBb, with a biphasic AP phase plot) compared with putative anaxonic DA cells (OBm, with a monophasic AP planar phase plot; Figure 2B, Table 2, example phase plots in Figure 4A). Echoing the soma area differences reported in Figure 1E, we found that membrane capacitance – a measure of the amount of plasma membrane – was overall significantly lower in OB than in midbrain DA neurons, once more indicating that OB neurons are smaller in size (Figure 2C, Table 2). Within the midbrain, we found that SNC and VTA neuron capacitance was not significantly different, despite the difference in soma size; this might reflect differences in the dendritic tree (Montero et al., 2021). Within the OB the putative anaxonic OBm neurons had lower capacitance value, results in line with consistent reports of them being the smallest population (Chand et al., 2015; Galliano et al., 2018; Korshunov et al., 2020; Kosaka et al., 2020) (Figure 2C, Table 2). Passive membrane resistance (Ri), a measure of the number of ion channels open at rest, was not different between the two brain areas, and there was no significant difference between SNC and VTA DA neurons. However, Ri was significantly higher in OBm than OBb neurons, indicating a less active and more electrotonically compact neuronal subtype (Figure 2D, Table 2). Together, these data indicate that OB DA neurons are smaller than midbrain DA neurons and have a higher membrane resistance, but a similar resting membrane potential.

3.3 | Voltage sag responses to hyperpolarisation are stronger in midbrain than forebrain OB DA neurons

In the midbrain, identification of DA neurons is often determined in voltage clamp by the presence of a hyperpolarisation-activated cation current ($I_{h,}$ or current sag), which plays a pivotal role in controlling intrinsic excitability (Neuhoff et al., 2002). In current clamp recordings, the time- and voltage-dependent opening of HCN channels results in a slow depolarising response (steady-state) to a triggered hyperpolarisation (peak), referred to as a voltage sag. By injecting hyperpolarising current steps in the four DA groups, we found no

TABLE 1 Morphological properties of DA cells.

DAT-tdTomato CELLS MORPHOLOGY						
	SNC (mean ± SEM, [n = 656])	**VTA (mean ± SEM, [n = 688])**	**SNC vs VTA nested t-test *p*-value**	**MB (mean ± SEM, [n = 1344])**	**FB (OB) (mean ± SEM, [n = 2337])**	**FB vs. MB nested t-test *p*-value**
Shape descriptors						
Area (μm^2)	233.10 ± 3.23	163.6 ± 2.33	0.03	197.5 ± 2.19	81.04 ± 0.67	0.0006
Area distributions (all not Gaussian, D'Agostino Pearson $p < 0.001$):						
• CV	0.35	0.37			0.37	
• Skewness	0.71	1.36			1.85	
• Kurtosis	0.81	3.86			6.33	
Max diameter (μm)	23.97 ± 0.23	19.93 ± 0.18	0.02	21.64 ± 0.16	13.05 ± 0.06	0.0002
Roundness	0.61 ± 0.01	0.66 ± 0.01	0.003	0.64 ± 0.01	0.71 ± 0.01	0.02
Cell density						
Density/μm^3 — overall	8.08×10^{-5}	7.04×10^{-5}	0.76	7.56×10^{-5}	11.74×10^{-5}	0.19

Mean values ± SEM of cell shape descriptors and cell density for DAT-tdTomato positive cells across forebrain OB and midbrain [N = 4]. Statistical differences were calculated with a mixed model t-test nested on mouse (SNC vs VTA for within the midbrain; SNC + VTA vs OB for across brain areas). Normality of the soma area distributions was calculated with a D'Agostino Pearson Omnibus test; CV = coefficient of variation; compared with a Gaussian distribution (0 skewness and 0 kurtosis) a positive skew indicates distribution with a longer right tail and a positive kurtosis indicates a distribution with more values in the tails. Grey shading indicates statistically significant difference. Individual data points and example images are presented in Figure 1.

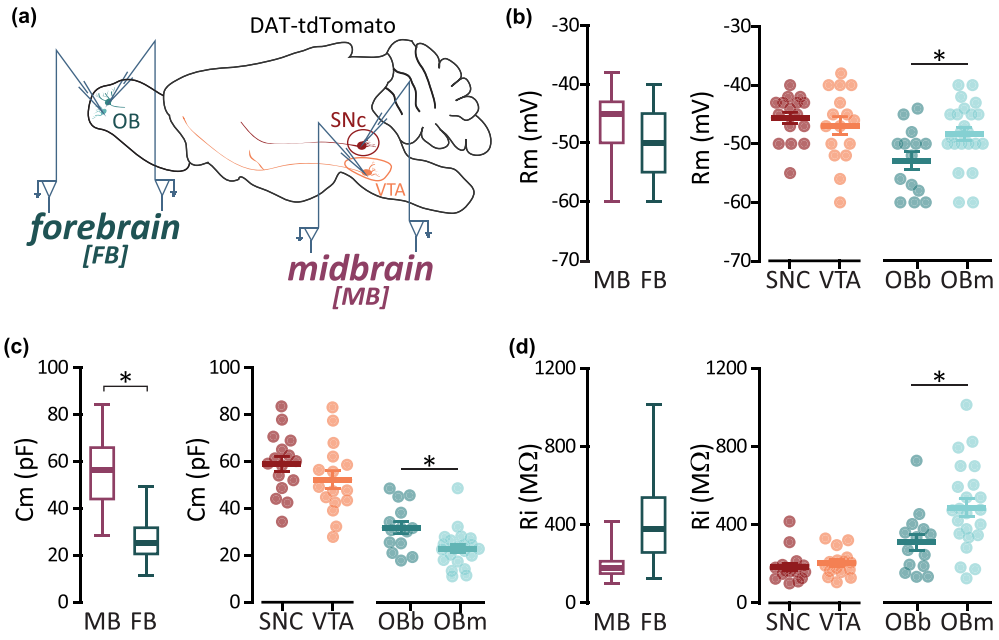

FIGURE 2 Passive electrical properties differ between forebrain OB and midbrain, and between the two subpopulations of OB DA neurons. (a) Schematic representation of the location of OB DA neurons in the forebrain OB and VTA and SNC DA neurons in the midbrain, targeted for whole cell patch clamp recordings in acute horizontal brain slices from juvenile DAT-tdTomato mice. (b) Resting membrane potential (Rm) in midbrain (SNC n = 16, VTA n = 16) and forebrain (OBb n = 14, OBm n = 23) neurons overall (left) and divided by subtype (right). (c–d). As in B, for membrane capacitance (cm) and input resistance (Ri). Circles are individual cells, lines are mean ± SEM, *$p < 0.05$; further quantification and statistical analysis in Table 2.

differences in the instantaneous hyperpolarisation (minimum voltage peak) between forebrain OB and midbrain. The difference between minimum voltage and steady-state voltage – the voltage sag amplitude – was significantly larger in midbrain DA neurons and indeed was typically less than 10 mV in OB DA neurons. The ratio between steady-state and peak voltage corrected for holding voltage – the sag index (Angelo et al., 2012) – was significantly smaller in midbrain DA neurons than in OB cells (Figure 3; Table 2). This is consistent with a larger voltage sag in midbrain DA neurons.

In line with previous data from rats (Pignatelli et al., 2013), the two subtypes of murine OB neurons displayed similarly shallow voltage sags, or no sag at all. Conversely, within the midbrain, we found higher sag indexes – and a trend towards higher sag amplitudes – in more SNC than VTA cells, which once more displayed more heterogeneity (Figure 3C–D; Table 2; sag amplitude coefficient of variation [CV] in SNC = 0.18, VTA = 0.54). Finally, we quantified the percentage of cells firing rebound APs following a hyperpolarisation-induced voltage sag. While approximately half of all OB DA neurons fired on rebound (57% of OBb, 48% of OBm), almost no midbrain DA neuron generated an AP following the end of the hyperpolarising step (SNC 6%, VTA 0%; χ^2 test, $p < 0.001$; Figure 3E). Taken together, these data show that SNC midbrain DA neurons have the largest voltage sag, followed by VTA DA neurons. Conversely, OB neurons of both categories have small voltage sags but are likely to fire rebound APs following a sustained hyperpolarisation. The ionic basis of the voltage sag and the rebound firing was not determined.

3.4 | Action potential waveforms are similar in forebrain OB and midbrain DA neurons

To analyse the properties of individual APs fired at threshold, we injected 10 ms depolarising current steps of increasing amplitude in the four groups of DA neurons (Figure 4A). Individual APs in forebrain OB and midbrain DA neurons were remarkably similar, showing no overall differences in voltage and injected current density threshold, and width at half-height (Figure 4B, C, F, Table 2). The lack of difference between OB and midbrain for AP current threshold might be explained by the large variance in the data obtained from VTA DA neurons (interquartile range SNC = 3.6pA/pF, VTA = 10.2pA/pF, OBb = 2.2pA/pF, OBm = 1.2pA/pF; Figure 4B), likely reflecting the heterogeneity of this population. AP onset rapidness, which we used to classify the OB subtypes

TABLE 2 Electrophysiological properties of DA cells.

DAT-tdTomato CELLS PHYSIOLOGY									
	MB mean ± SEM	**FB mean ± SEM**	**MB vs FB nested t-test *p*-value**	**SNC mean ± SEM**	**VTA mean ± SEM**	**SNC vs VTA test type, *p*-value**	**OBb mean± SEM**	**OBm mean ± SEM**	**OBb vs OBm test type, *p*-value**
PASSIVE PROPERTIES									
Resting potential (mV)	−46.25 ± 0.91	−50.03 ± 0.96	0.15	−45.56 ± 0.99	−46.94 ± 1.54	t, 0.46	−52.86 ± 1.49	−48.30 ± 1.13	t, 0.02
Membrane capacitance (pF)	55.82 ± 2.53	26.35 ± 1.57	0.04	59.31 ± 3.25	52.33 ± 3.79	t, 0.17	31.85 ± 2.62	23.00 ± 1.64	MW, 0.01
Input resistance (mΩ)	194 ± 13	420 ± 35	0.15	184 ± 20	204 ± 17	MW, 0.19	310 ± 43	488 ± 46	MW, 0.01
SAG VOLTAGE									
Min voltage (peak, mV)	−105 ± 0.7	−106 ± 1.2	0.78	−103 ± 0.9	−106 ± 1.0	MW, 0.14	−103 ± 1.5	−107 ± 1.5	MW, 0.01
Steady state (mV)	−86 ± 1.6	−100 ± 0.8	0.06	−82 ± 1.4	−90 ± 2.5	t, 0.02	−99 ± 1.3	−101 ± 1.1	MW, 0.21
Sag amplitude (mV)	18.71 ± 1.27	5.49 ± 0.67	0.04	21.39 ± 0.98	16.03 ± 2.17	MW, 0.07	4.05 ± 0.58	6.37 ± 0.98	MW, 0.15
Sag index	0.58 ± 0.03	0.89 ± 0.02	0.046	0.51 ± 0.03	0.65 ± 0.05	tW, 0.02	0.91 ± 0.93	0.87 ± 0.02	tW, 0.11
ACTION POTENTIAL PROPERTIES									
Threshold (pA/pF)	11.44 ± 1.14	3.23 ± 0.21	0.15	7.80 ± 0.65	15.09 ± 1.79	tW, 0.001	2.37 ± 0.37	3.75 ± 0.18	tW, 0.004
Threshold (mV)	−35.85 ± 1.13	−36.65 ± 0.54	0.64	−37.04 ± 1.44	−34.66 ± 1.74	MW, 0.30	−38.34 ± 0.99	−35.61 ± 0.52	t, 0.01
Onset rapidness (1/ms)	17.69 ± 1.06	5.05 ± 0.56	0.05	17.77 ± 1.70	17.60 ± 1.34	t, 0.93	8.595 ± 0.81	2.88 ± 0.18	n/a
Peak amplitude (mV)	33.81 ± 2.08	47.56 ± 1.08	0.09	29.46 ± 3.13	38.17 ± 2.38	t, 0.03	47.64 ± 1.74	47.51 ± 1.41	t, 0.96
Width at half-height (ms)	0.78 ± 0.03	0.76 ± 0.02	0.68	0.76 ± 0.04	0.79 ± 0.04	t, 0.60	0.69 ± 0.03	0.80 ± 0.03	t, 0.03
After hyperpolarisation (AHP, mV)	−27.98 ± 1.11	−39.67 ± 0.87	0.06	−25.37 ± 1.26	−30.58 ± 1.61	t, 0.02	−38.15 ± 1.60	−40.60 ± 0.98	t, 0.17
REPETITIVE FIRING PROPERTIES									
Max number of APs	7.63 ± 1.04	25.17 ± 2.01	0.03	5.69 ± 0.41	9.43 ± 1.87	MW, 0.02	27.79 ± 2.74	22.73 ± 2.87	t, 0.21
First AP delay (ms)	267 ± 22	109 ± 21	0.15	202 ± 19	327 ± 30	t, 0.002	136 ± 34	83 ± 23	MW, 0.14
Inter-spike interval CV	0.47 ± 0.04	0.19 ± 0.02	0.05	0.53 ± 0.06	0.42 ± 0.06	t, 0.17	0.15 ± 0.02	0.22 ± 0.04	MW, 0.11
Max AP frequency (Hz)	51.59 ± 5.53	75.38 ± 5.41	0.29	66.85 ± 8.44	37.42 ± 4.98	t, 0.01	67.76 ± 7.01	82.50 ± 7.95	t, 0.18
Slope I/O curve (Hz/(pA/pF)	3.17 ± 0.85	7.94 ± 0.51	0.08	4.61 ± 1.66	1.82 ± 0.38	MW, 0.02	8.14 ± 0.77	7.75 ± 0.70	t, 0.71

Mean values ± SEM of passive properties, sag currents, action potential properties (SNC n = 16, VTA n = 16, OBb n = 14, OBm n = 23) and repetitive firing properties (SNC n = 13, VTA n = 14, OBb n = 14, OBm n = 15) for DA cells across forebrain OB and midbrain. Statistical differences between brain areas (forebrain OB vs. midbrain) were calculated with a mixed model t-test nested on sub-region. Within each brain region, differences between sub-regions groups were calculated independently with an unpaired t-test for normally-distributed data ('t' for data with equal variance, 'tW' for data with unequal variance and Welch correction) or with a Mann–Whitney test for non-normally distributed data ('MW'). Grey shading indicates statistically significant difference. Individual data points and example traces are presented in Figures 2–5.

given the characteristically low values in the OBm cells lacking the axon initial segment initiation site, was not significantly different (Figure 4D, $p = 0.05$). Likewise, AP and AHP peak amplitudes were also not statistically different in the OB (Figure 4E, G, Table 2).

When we analysed differences within each brain area, we confirmed that the putative axon-bearing OBb DA cells require less current and a less depolarised voltage than their putative-anaxonic OBm counterparts to fire an AP (Figure 4B–G, Table 2). Within the midbrain, we found marked differences in terms of firing threshold (half the injected current density needed in SNC vs. VTA cells), and AP shape with lower peak and AHP amplitudes in SNC than VTA (Figure 4B–G, Table 2).

Overall, these data suggest that a similar but not identical complement of voltage-gated ion changes underlie the AP in all four neuronal types. Notably, all four classes of DA neurons have large amplitude AHPs (Figure 4G).

3.5 | Repetitive action potential firing differs between forebrain OB and midbrain

Despite the similarity in their AP waveforms, forebrain OB and midbrain DA neurons displayed remarkably different repetitive firing properties when probed with 500 ms-long current injections of increasing intensity (Figure 5A–E). To allow for inter-area comparisons despite the substantial differences in cell size, we normalised current injections for cell capacitance (i.e., current density) and confirmed different I-O curves between the midbrain and OB DA neurons, and at high current densities between the two OB subtype (Figure 5F, mixed-model ANOVA, effect of manipulation $F_{1.38,\ 56} = 82.16$, $p < 0.001$, effect of time $F_{3,\ 52} = 28.69$, $p < 0.001$; effect manipulation × time $F_{27,\ 376} = 14.36$, $p < 0.001$; OBb vs. OBm for injected current>5.5pA/pF, $p < 0.05$). The most striking difference between forebrain OB and midbrain DA cells' repetitive firing was the maximum number of APs fired within the injection window, which was over three times larger in the OB than in the midbrain (Figure 5G, Table 2). While the timing of the first AP is squarely similar in OB and midbrain DA neurons (Figure 5H), the inter-spike interval coefficient of variation (ISI CV) was lower for the OB (Figure 5I, $p = 0.048$). The overall higher excitability in the OB as measured by maximum number of APs was mirrored in a strong trend towards a higher slope of the current density versus AP frequency I-O curve (Figure 5J–K, Table 2, $p = 0.08$).

While we only found differences between the two OB DA subtypes at high current injections (but reported strong trends towards OBb being overall more excitable), we observed that SNC and VTA differ in almost all parameters (Figure 5G–K, Table 2). Of note once more is the variability observed in VTA: for instance, while most midbrain neurons fired less than 10 APs, one VTA neuron fired a maximum of 30 spikes (interquartile range SNC = 1.5, VTA = 4; coefficient of variation SNC = 0.26, VTA = 0.74).

3.6 | Principal component analysis highlights consistent grouping of midbrain versus forebrain OB subtypes

Finally, to understand the overall impact of the various individual electrophysiological features reported above, we performed PCA (see Materials and Methods for details). The first two principal components (PC) accounted for 43.16% and 13.94% of the variance, respectively (Figure 6A–B). Plotting the primary and secondary component scores for each neuron against each other revealed clear clustering of forebrain OB and midbrain DA neurons (Figure 6A). To determine whether a specific set of electrophysiological properties predominantly contributed to PC1 and PC2, we graphed loading scores (derived from eigenvalues and eigenvectors) for each PC and found no clear-cut major single source of variation (Figure 6C). To further confirm that no single experimental protocol – passive properties, voltage sag, AP shape, repetitive firing – alone drove the variability in the dataset, we performed two additional PCAs. The first included only measurements derived from single and repetitive AP firing protocols and once more returned two clear midbrain versus forebrain OB clusters with PC1 and PC2 responsible for 42.64% and 17.82% of the variation, respectively (Figure 6D). Similarly, PCA of sag voltage measurements resulted in similar but clear clustering patterns (PC1: 63.30%; PC2: 33.60%; Figure 6E). Across all three PC analyses, we found some overlap between the midbrain and OB clusters (1–3 'misplaced' cells). This is perhaps unsurprising given the variability of electrophysiological properties, especially in VTA. In sum, although we found considerable overlap in individual intrinsic properties of DA neurons across the two brain areas, when all measurements are evaluated holistically, we found a clear functional split between forebrain OB and midbrain DA neurons.

4 | DISCUSSION

In this study, we compared the morphological and functional properties of midbrain and forebrain OB DA neurons identified via the expression of the fluorescent marker tdTomato under the control of the DAT promoter

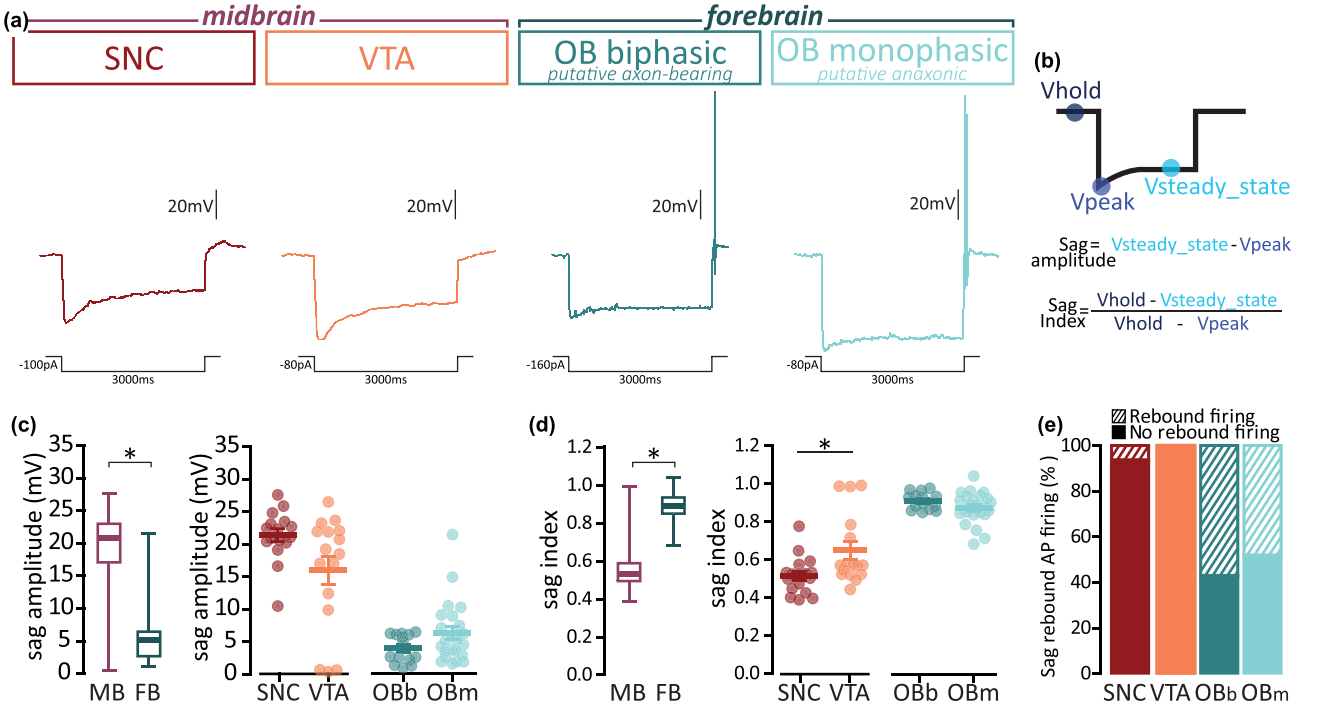

FIGURE 3 The depolarisation response to hyperpolarisation (sag potential) is consistently present in midbrain DA neurons, while it is small or absent in forebrain OB DA cells. (a) Example traces of the voltage sag response to hyperpolarising current injections in midbrain (SNC n = 16, VTA n = 16; left) and forebrain (OBb n = 14, OBm n = 23; right) DA neurons. (b) Schematic visualisation of the voltage sag analysis parameters and formulas used to calculate sag amplitude and index. (c) Voltage sag amplitude and (d) sag index in midbrain and forebrain OB neurons overall (left) and divided by subset (right). (e) Percentage of neurons firing an action potential (striped bars) after the rebound depolarisation following hyperpolarisation. Circles are individual cells, lines are mean ± SEM, *$p < 0.05$; further quantification and statistical analysis in Table 2.

(Bäckman et al., 2006). We demonstrated that within the midbrain, VTA and SNC DA neurons are only broadly similar in their AP waveform and repetitive firing properties, and that VTA DA neurons showed greater heterogeneity. We also confirmed previous findings that putative anaxonic/regenerating OB DA neurons are smaller and less excitable than their embryonic-born/axon-bearing counterparts (Galliano et al., 2018). Midbrain and forebrain OB DA neurons were significantly different in terms of sag voltage and excitability during repetitive firing. Moreover, our PCA indicates a clear separation of midbrain and forebrain OB DA neurons on a wide range of physiological parameters, indicating that DA neurons across brain regions do not share a common neurophysiological signature.

4.1 | Penetrance and specificity of the DAT-Cre line

Given that, to the best of our knowledge, this is the first study to use the DAT-Cre line to electrophysiologically profile midbrain DA neurons, we first characterised this reporter line against the gold standard of TH expression. Previous work showed incomplete penetrance and imperfect specificity in the OB (Byrne et al., 2022; Galliano et al., 2018), a finding that we replicated: 16% of TH positive neurons failed to express DAT, and 12% of DAT-expressing neurons did not express TH (a population that has been previously characterised as calretinin-positive and whose electrophysiological signatures clearly distinguishes them from DA cells (Byrne et al., 2022; Fogli Iseppe et al., 2016)). Conversely, in SNC and VTA, over 90% of DAT-tdTomato neurons co-stained for anti-TH antibodies, indicating that the DAT-Cre line captures most midbrain DA neurons with minimal leakage. One could speculate that such a discrepancy in DA neuron coverage between midbrain and OB with the DAT-Cre line can be caused by more abundant polymorphisms in the Slc6a3 gene and/or different allele dosage, as well as by the ectopic expression of the gene in the bulbar calretinin interneurons, and/or by more general differences in recombination efficiency across different tissues (Heffner et al., 2012; Stuber et al., 2015).

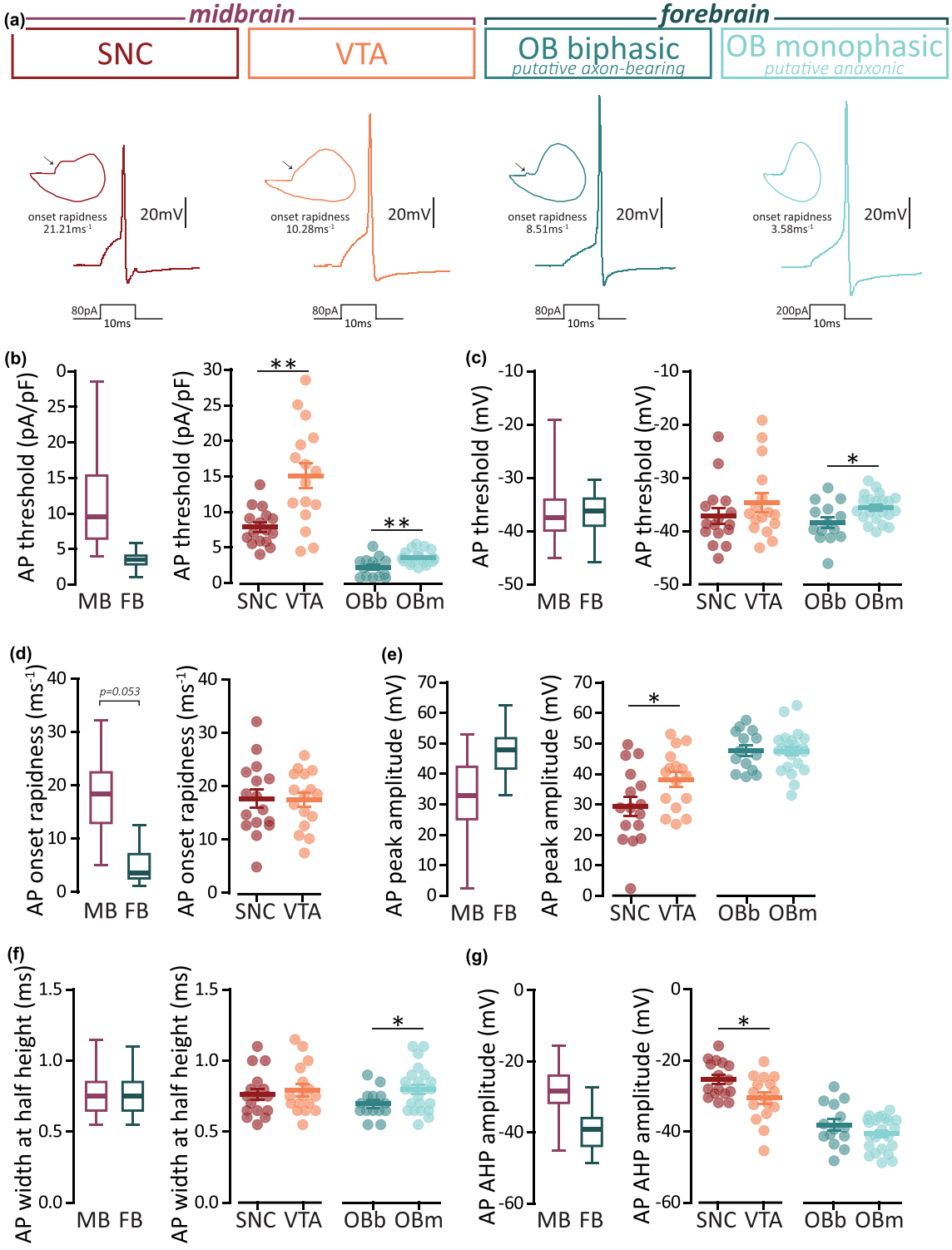

FIGURE 4 Action potential waveforms are largely similar across forebrain OB and midbrain DA neurons, but vary substantially between SNC and VTA. (a) Example traces of the membrane voltage response to the minimum depolarising 10 ms-long current injection needed to evoke an AP in midbrain (SNC n = 16, VTA n = 16; left) and forebrain (OBb n = 14, OBm n = 23; right) DA neurons. Arrow on the planar phase plots points to the axon initial segment-dependent first AP phase. Waveform parameters for midbrain and forebrain OB neurons overall (left) and divided by subset (right) include (b) injected current density needed to evoke an AP, (c) membrane potential at which the AP was evoked, (d) AP rate of rise from threshold (onset rapidness), (e) AP peak membrane potential, (f) AP width at half the maximum height, and (g) peak amplitude of the AP after-hyperpolarisation (AHP). Circles are individual cells, lines are mean ± SEM, $^{*}p < 0.05$; $^{**}p < 0.01$, further quantification and statistical analysis in Table 2.

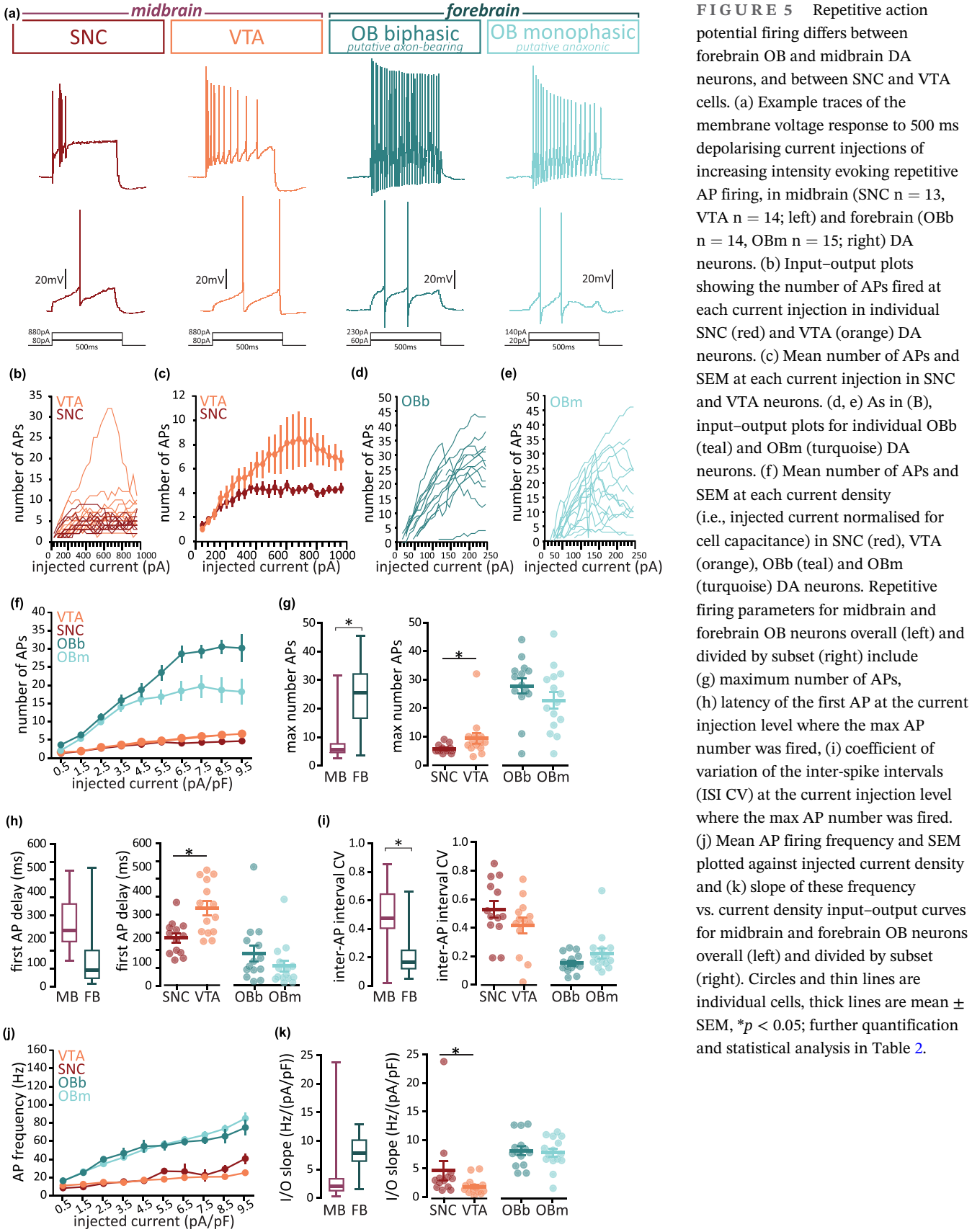

FIGURE 5 Repetitive action potential firing differs between forebrain OB and midbrain DA neurons, and between SNC and VTA cells. (a) Example traces of the membrane voltage response to 500 ms depolarising current injections of increasing intensity evoking repetitive AP firing, in midbrain (SNC n = 13, VTA n = 14; left) and forebrain (OBb n = 14, OBm n = 15; right) DA neurons. (b) Input–output plots showing the number of APs fired at each current injection in individual SNC (red) and VTA (orange) DA neurons. (c) Mean number of APs and SEM at each current injection in SNC and VTA neurons. (d, e) As in (B), input–output plots for individual OBb (teal) and OBm (turquoise) DA neurons. (f) Mean number of APs and SEM at each current density (i.e., injected current normalised for cell capacitance) in SNC (red), VTA (orange), OBb (teal) and OBm (turquoise) DA neurons. Repetitive firing parameters for midbrain and forebrain OB neurons overall (left) and divided by subset (right) include (g) maximum number of APs, (h) latency of the first AP at the current injection level where the max AP number was fired, (i) coefficient of variation of the inter-spike intervals (ISI CV) at the current injection level where the max AP number was fired. (j) Mean AP firing frequency and SEM plotted against injected current density and (k) slope of these frequency vs. current density input–output curves for midbrain and forebrain OB neurons overall (left) and divided by subset (right). Circles and thin lines are individual cells, thick lines are mean ± SEM, $*p < 0.05$; further quantification and statistical analysis in Table 2.

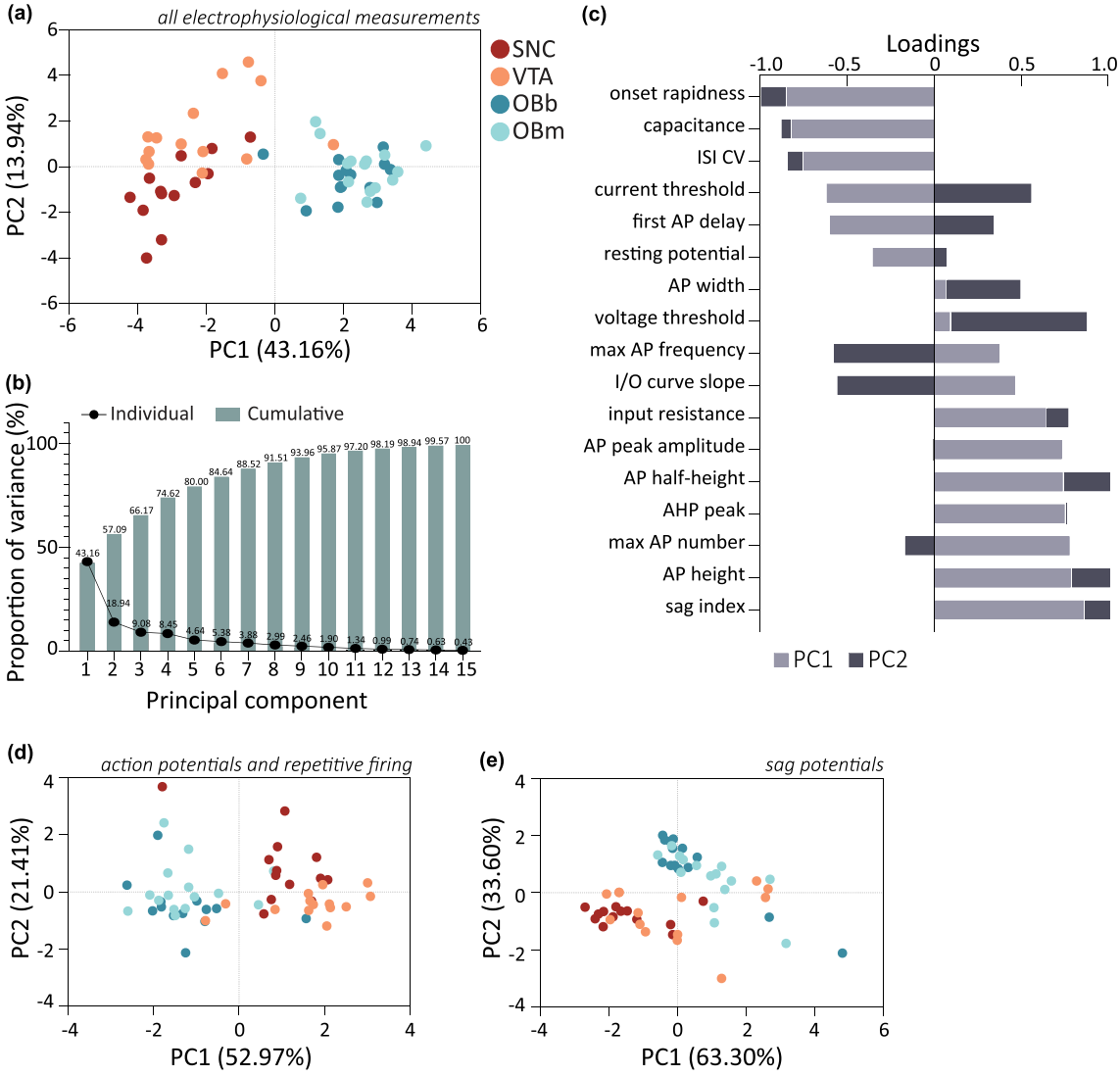

FIGURE 6 Principal component analysis (PCA) of electrophysiological properties reveals clear clustering of midbrain and forebrain OB DA neurons. (a) PC score plot for forebrain (OBb, teal, n = 14; OBm, turquoise, n = 15) and midbrain (SNC, red, n = 13; VTA, orange, n = 14) DA neurons based on all measurements obtained from whole-cell recordings (Figures 2–5, Table 2). Each circle represents a cell plotted against its primary and secondary principal component (PC) scores. (b) Individual and cumulative proportion of variance explained by each principal component. (c) Loading scores for all variables showing their respective contributions to PC1 (light grey) and PC2 (dark grey). (d-e) As in C, but for PCA including only measurements from single AP + repetitive firing (Figures 4–5) and sag potentials (Figure 3), respectively.

4.2 | Morphological and functional heterogeneity of midbrain DA neurons

A plethora of circuit functions and behavioural roles has been attributed to midbrain DA neurons (Berke, 2018), and it is now accepted that such range at the systems level is matched by a similar breadth at the molecular and cellular level (Garritsen et al., 2023). In vivo, synaptic inputs enable midbrain DA neurons to fire APs in bursting and irregular patterns (Grace & Bunney, 1984), but the strong influence of intrinsic ion channels, including Ca^{2+}-activated small conductance K^+ channels, imposes a more regular firing pattern ex vivo (de Vrind et al., 2016; Kang & Kitai, 1993; Khaliq & Bean, 2008, 2010; Neuhoff et al., 2002; Puopolo et al., 2007; Wolfart et al., 2001), with marked differences between SNC and VTA DA neurons (reviewed by Gantz et al., 2018). Across the various protocols assessing passive and active electrophysiological properties, our DAT-tdTomato mouse SNC recordings compare well with previously published rat data (Pucak & Grace, 1996). Similarly, the VTA results from genetically tagged mouse DA neurons are broadly in line with recordings of rat VTA DA neurons defined by TH and I_h expression (Margolis et al., 2006), including

a similar soma size and passive properties, as well as comparable AP waveforms. With the current step protocol that we employed, VTA DA neurons fired a maximum of ~9 spikes at a maximum frequency of ~37 Hz, higher than spontaneous spike firing frequency (1–10 Hz; Margolis et al., 2006; Ungless & Grace, 2012). Given that the majority of our VTA recordings were in the ventral tier, where neurons are known to fire at higher frequencies than their dorsal counterparts (Lammel et al., 2008), such discrepancy can be explained by a sampling difference as well as by the different evoked versus spontaneous firing configuration. Importantly, our ex vivo results are consistent with the high frequency phasic firing seen during reward prediction error learning (Schultz, 2016) and with the heterogeneity extensively reported in the literature (Morales & Margolis, 2017). Indeed, our data likely under-represent the heterogeneity of DA neurons as ~15% of VTA TH positive neurons were not DAT positive (Figure 1), and in SNC we focused around MT. We have not recorded from DA neurons with undetectable levels of DAT (Lammel et al., 2008), or those in the lateral SNC.

Intra-group heterogeneity notwithstanding, we found substantial differences when we compared SNC with VTA neurons in DAT-tdTomato mice. Overall, our data show that SNC DA neurons have a larger and more oblong soma but are, nevertheless, more excitable than VTA DA cells when the injected current was normalised for cell capacitance. Compared with VTA neurons, SNC APs were fired at lower thresholds but had a smaller peak and AHP amplitude, and the AP number plateaued rapidly when the neurons were probed with prolonged current injections. Taken together with the consistently larger voltage sag in SNC DA cells than in the VTA neurons, our results indicate that the two midbrain subtypes are equipped with a different complement of voltage-gated channels, and that within each subgroup, such complement is varied and allows for the observed heterogeneity of both AP and sag voltage properties.

4.3 | Midbrain versus forebrain OB DA neurons

Forebrain OB DA neurons are a handful of cells that makes up a very small fraction of both bulbar inhibitory interneurons and DA neurons overall — yet, even in their scarcity, they display extreme diversity in terms of developmental profile, shape, and function (Bonzano et al., 2016; Chand et al., 2015; Galliano et al., 2018; Kosaka et al., 2020). Our results confirm that using the AP rate of rise and bi- or mono-phasic nature of the planar phase plot allows for a clear split between putative-anaxonic and putative-axon bearing, with the latter being larger and more excitable. To compare the repetitive firing of large but less excitable midbrain DA neurons with the smaller but more excitable forebrain OB ones, we skewed our injected current steps to higher values than in our previous studies (Galliano et al., 2018, 2021). While this dataset thus lacks the granularity to finely sample firing behaviour around threshold, it confirmed that at high-injected current densities, OBb DA neurons had a faster-rising I-O curve than OBm cells, in line with their overall higher excitability.

The two OB subtypes have similarly shallow voltage sags, with values at times so low that they cease to be sags altogether (Pignatelli et al., 2013). This is a very interesting difference between forebrain OB and midbrain DA cells, since the presence of a voltage sag and I_h current have long been considered a signature of the DA phenotype, so much so that it was often used to identify them before the advent of transgenic mouse lines (Ungless & Grace, 2012). Furthermore, while OB and midbrain DA cells have largely similar AP waveforms, their repetitive firing behaviour is substantially different. Specifically, OB DA neurons of either subtype fired over thrice the number of APs than midbrain DA cells over a 500 ms current injection window and did so with a much more regular temporal profile. In line with data from hippocampal pyramidal neurons (Hewitt et al., 2021), one could hypothesise that the more prominent sag in the midbrain gears the DA neurons towards a faster-adapting repetitive firing. This could be neuroprotective especially for those cells located in the ventral midbrain which co-transmit glutamate, and perhaps unneeded in the GABA-co-transmitting OB DA cells (Vaaga et al., 2014; Wallace & Sabatini, 2023). An important potential difference is the presence of D2 dopamine receptors. These are well-documented in midbrain DA neurons (albeit with some variation; (Chiodo et al., 1984)), where they auto-inhibit DA neuron firing. It remains unclear whether they are expressed on OB DA neurons of both/either subtypes, and what their effects, if any, on firing are (Gutièrrez-Mecinas et al., 2005).

Our PCA unexpectedly showed that overall, the large, embryonic-born, axon-bearing OB DA cells are less similar to large, embryonic-born, axon-bearing midbrain DA cells than to their small, regenerating, anaxonic OB counterparts. Indeed, the striking heterogeneity that we described within each subgroup and each brain area is, nonetheless, overruled by the even larger differences in size, shape and electrophysiological properties of DA neurons between OB and midbrain. Such findings highlight the challenges faced by stem cell replacement strategies such as harvesting adult neural stem cells of the subventricular zone, precursors of the OB DA cells, and transplanting them in

Parkinsonian animals (Cave et al., 2014). Regenerating OB neurons are anaxonic and can therefore be only transplanted directly into the striatum, not in the SNC. Moreover, even if they could manage to complete their differentiation and connect within the striatal network, they would likely fire more APs than SNC neurons. Therefore, their net effect on striatal processing may not be suitable to replace the lost SNC DA drive.

4.4 | Not all dopaminergic neurons are created equal

Is there a common set of functional properties that makes a neuron DA? Our PCA does not support this idea. Research investigating all DA groups within the brain has been steadily accumulating, with each new study revealing an increasing level of heterogeneity. While in this study we did not record from the retina and hypothalamic DA groups, others have highlighted how those neurons too are molecularly, morphologically and functionally diverse (Hirasawa et al., 2015; Korchynska et al., 2022; Romanov et al., 2017; Zhang et al., 2007). Moreover, DA heterogeneity seems to be an evolutionarily conserved feature across phyla, with reports in both other vertebrates such as the zebrafish (Caldwell et al., 2019; McLean & Fetcho, 2004) and invertebrates such as drosophila (Ma et al., 2023; Otto et al., 2020). So, what defines a DA neuron? Perhaps we ought to consider DA neurons just as varied as 'typical' neurons (Cerminara et al., 2015; Morgan et al., 2016; Tasic et al., 2016). However, albeit diverse, they share a common feature: dopamine. This allows them to exert an enhanced level of temporal and spatial control on their postsynaptic targets, thereby supporting an extensive array of behavioural functions.

AUTHOR CONTRIBUTIONS

Maggy Yu Hei Lau: Data curation; formal analysis; investigation; validation. **Sana Gadiwalla:** Data curation; formal analysis; validation; visualization; writing—review and editing. **Susan Jones:** Conceptualization; data curation; formal analysis; funding acquisition; project administration; supervision; writing—original draft; writing—review and editing. **Elisa Galliano:** Conceptualization; data curation; formal analysis; funding acquisition; investigation; project administration; supervision; visualization; writing—original draft; writing—review and editing.

ACKNOWLEDGEMENTS

This work was supported by the Royal Society Research (RGS\R1\19148), the URKI Biotechnology and Biological Sciences Research Council (BBSRC) (BB\W014688\1) and the Newton Trust ISSF Grant to EG, and two Physiology, Development and Neuroscience Departmental Research Grants to SJ and EG. We wish to thank Matthew Grubb for antibodies and access to his lab's confocal microscope, to Ailie McWhinnie for comments on the manuscript, and all members of the Galliano laboratory for providing helpful discussions.

CONFLICT OF INTEREST STATEMENT

The authors declare no financial or personal relationship that could be construed as a potential conflict of interest.

PEER REVIEW

The peer review history for this article is available at https://www.webofscience.com/api/gateway/wos/peer-review/10.1111/ejn.16239.

DATA AVAILABILITY STATEMENT

The full dataset can be found on the University of Cambridge Apollo repository (https://doi.org/10.17863/CAM.102763) under a CC-BY license.

ORCID

Sana Gadiwalla https://orcid.org/0009-0008-1783-3734
Susan Jones https://orcid.org/0000-0002-4130-8111
Elisa Galliano https://orcid.org/0000-0002-6941-766X

REFERENCES

Aarts, E., Verhage, M., Veenvliet, J. V., Dolan, C. V., & van der Sluis, S. (2014). A solution to dependency: Using multilevel analysis to accommodate nested data. *Nature Neuroscience*, *17*, 491–496. https://doi.org/10.1038/nn.3648

Andén, N. E., Dahlström, A., Fuxe, K., & Larsson, K. (1965). Mapping out of catecholamine and 5-hydroxytryptamine neurons innervating the telencephalon and diencephalon. *Life Sciences*, *4*, 1275–1279. https://doi.org/10.1016/0024-3205(65)90076-7

Angelo, K., Rancz, E. A., Pimentel, D., Hundahl, C., Hannibal, J., Fleischmann, A., Pichler, B., & Margrie, T. W. (2012). A biophysical signature of network affiliation and sensory processing in mitral cells. *Nature*, *488*, 375–378. https://doi.org/10.1038/nature11291

Bäckman, C. M., Malik, N., Zhang, Y., Shan, L., Grinberg, A., Hoffer, B. J., Westphal, H., & Tomac, A. C. (2006). Characterization of a mouse strain expressing Cre recombinase from the 3′ untranslated region of the dopamine transporter locus. *Genesis*, *44*, 383–390. https://doi.org/10.1002/dvg.20228

Banerjee, A., Marbach, F., Anselmi, F., Koh, M. S., Davis, M. B., Garcia da Silva, P., Delevich, K., Oyibo, H. K., Gupta, P., Li, B., & Albeanu, D. F. (2015). An Interglomerular circuit gates glomerular output and implements gain control in the mouse olfactory bulb. *Neuron*, *87*, 193–207. https://doi.org/10.1016/j.neuron.2015.06.019

Berke, J. D. (2018). What does dopamine mean? *Nature Neuroscience*, *21*, 787–793. https://doi.org/10.1038/s41593-018-0152-y

Bissonette, G. B., & Roesch, M. R. (2016). Development and function of the midbrain dopamine system: What we know and

what we need to: Development and function of the dopamine system. *Genes, Brain and Behavior*, *15*, 62–73. https://doi.org/10.1111/gbb.12257

Björklund, A., & Dunnett, S. B. (2007). Dopamine neuron systems in the brain: An update. *Trends in Neurosciences*, *30*, 194–202. https://doi.org/10.1016/j.tins.2007.03.006

Bonzano, S., Bovetti, S., Gendusa, C., Peretto, P., & De Marchis, S. (2016). Adult born olfactory bulb dopaminergic interneurons: Molecular determinants and experience-dependent plasticity. *Frontiers in Neuroscience*, *10*, 189. https://doi.org/10.3389/fnins.2016.00189

Byrne, D. J., Lipovsek, M., Crespo, A., & Grubb, M. S. (2022). Brief sensory deprivation triggers plasticity of dopamine-synthesising-enzyme expression in genetically labelled olfactory bulb dopaminergic neurons. *European Journal of Neuroscience*, *56*, 3591–3612. https://doi.org/10.1111/ejn.15684

Caldwell, L. J., Davies, N. O., Cavone, L., Mysiak, K. S., Semenova, S. A., Panula, P., Armstrong, J. D., Becker, C. G., & Becker, T. (2019). Regeneration of dopaminergic neurons in adult zebrafish depends on immune system activation and differs for distinct populations. *The Journal of Neuroscience*, *39*, 4694–4713. https://doi.org/10.1523/JNEUROSCI.2706-18.2019

Cave, J. W., Wang, M., & Baker, H. (2014). Adult subventricular zone neural stem cells as a potential source of dopaminergic replacement neurons. *Frontiers in Neuroscience*, *8*, 16. https://doi.org/10.3389/fnins.2014.00016

Cerminara, N. L., Lang, E. J., Sillitoe, R. V., & Apps, R. (2015). Redefining the cerebellar cortex as an assembly of non-uniform Purkinje cell microcircuits. *Nature Reviews. Neuroscience*, *16*, 79–93. https://doi.org/10.1038/nrn3886

Chand, A. N., Galliano, E., Chesters, R. A., & Grubb, M. S. (2015). A distinct subtype of dopaminergic interneuron displays inverted structural plasticity at the axon initial segment. *The Journal of Neuroscience*, *35*, 1573–1590. https://doi.org/10.1523/JNEUROSCI.3515-14.2015

Chinta, S. J., & Andersen, J. K. (2005). Dopaminergic neurons. *The International Journal of Biochemistry & Cell Biology*, *37*(5), 942–946. https://doi.org/10.1016/j.biocel.2004.09.009

Chiodo, L. A., Bannon, M. J., Grace, A. A., Roth, R. H., & Bunney, B. S. (1984). Evidence for the absence of impulse-regulating somatodendritic and synthesis-modulating nerve terminal autoreceptors on subpopulations of mesocortical dopamine neurons. *Neuroscience*, *12*, 1–16. https://doi.org/10.1016/0306-4522(84)90133-7

Dahlstroem, A., & Fuxe, K. (1964). Eevidence for the existence of monoamine-containing neurons in the central nervous system. I. Demonstration of monoamines in the cell bodies of brain stem neurons. *Acta Physiologica Scandinavica. Supplementum*, *232*, 1–55.

de Vrind, V., Scuvée-Moreau, J., Drion, G., Hmaied, C., Philippart, F., Engel, D., & Seutin, V. (2016). Interactions between calcium channels and SK channels in midbrain dopamine neurons and their impact on pacemaker regularity: Contrasting roles of N- and L-type channels. *European Journal of Pharmacology*, *788*, 274–279. https://doi.org/10.1016/j.ejphar.2016.06.046

Deleidi, M., Cooper, O., Hargus, G., Levy, A., & Isacson, O. (2011). Oct4-induced reprogramming is required for adult brain neural stem cell differentiation into midbrain dopaminergic neurons. *PLoS ONE*, *6*, e19926. https://doi.org/10.1371/journal.pone.0019926

Economo, M. N., Hansen, K. R., & Wachowiak, M. (2016). Control of mitral/tufted cell output by selective inhibition among olfactory bulb glomeruli. *Neuron*, *91*, 397–411. https://doi.org/10.1016/j.neuron.2016.06.001

Fogli Iseppe, A., Pignatelli, A., & Belluzzi, O. (2016). Calretinin-Periglomerular interneurons in mice olfactory bulb: Cells of few words. *Frontiers in Cellular Neuroscience*, *10*, 231. https://doi.org/10.3389/fncel.2016.00231

Galliano, E., Franzoni, E., Breton, M., Chand, A. N., Byrne, D. J., Murthy, V. N., & Grubb, M. S. (2018). Embryonic and postnatal neurogenesis produce functionally distinct subclasses of dopaminergic neuron. *eLife*, *7*. https://doi.org/10.7554/eLife.32373

Galliano, E., Hahn, C., Browne, L. P., Villamayor, R., Tufo, C., Crespo, A., & Grubb, M. S. (2021). Brief sensory deprivation triggers cell type-specific structural and functional plasticity in olfactory bulb neurons. *The Journal of Neuroscience*, *41*, 2135–2151. https://doi.org/10.1523/JNEUROSCI.1606-20.2020

Galliano, E., Franzoni, E., Breton, M., Chand, A., Byrne, D., Murthy, V. N., & Grubb, M. (2019). Data from: Embryonic and postnatal neurogenesis produce functionally distinct subclasses of dopaminergic neuron [Dataset]. Dryad. https://doi.org/10.5061/dryad.b5hg8d6

Gantz, S. C., Ford, C. P., Morikawa, H., & Williams, J. T. (2018). The evolving understanding of dopamine neurons in the substantia Nigra and ventral tegmental area. *Annual Review of Physiology*, *80*, 219–241. https://doi.org/10.1146/annurev-physiol-021317-121615

Garritsen, O., van Battum, E. Y., Grossouw, L. M., & Pasterkamp, R. J. (2023). Development, wiring and function of dopamine neuron subtypes. *Nature Reviews. Neuroscience*, *24*, 134–152. https://doi.org/10.1038/s41583-022-00669-3

Grace, A. A., & Bunney, B. S. (1984). The control of firing pattern in nigral dopamine neurons: Burst firing. *The Journal of Neuroscience*, *4*, 2877–2890. https://doi.org/10.1523/JNEUROSCI.04-11-02877.1984

Greene, J. G. (2006). Gene expression profiles of brain dopamine neurons and relevance to neuropsychiatric disease. *The Journal of Physiology*, *575*, 411–416. https://doi.org/10.1113/jphysiol.2006.112599

Gutièrrez-Mecinas, M., Crespo, C., Blasco-Ibáñez, J. M., Gracia-Llanes, F. J., Marqués-Marí, A. I., Nácher, J., Varea, E., & Martínez-Guijarro, F. J. (2005). Distribution of D2 dopamine receptor in the olfactory glomeruli of the rat olfactory bulb. *The European Journal of Neuroscience*, *22*, 1357–1367. https://doi.org/10.1111/j.1460-9568.2005.04328.x

Halász, N., Johansson, O., Hökfelt, T., Ljungdahl, A., & Goldstein, M. (1981). Immunohistochemical identification of two types of dopamine neuron in the rat olfactory bulb as seen by serial sectioning. *Journal of Neurocytology*, *10*, 251–259. https://doi.org/10.1007/BF01257970

Heffner, C. S., Herbert Pratt, C., Babiuk, R. P., Sharma, Y., Rockwood, S. F., Donahue, L. R., Eppig, J. T., & Murray, S. A. (2012). Supporting conditional mouse mutagenesis with a comprehensive cre characterization resource. *Nature Communications*, *3*, 1218. https://doi.org/10.1038/ncomms2186

Hewitt, L. T., Ordemann, G. J., & Brager, D. H. (2021). High and low expression of the hyperpolarization activated current (I h)

in mouse CA1 stratum oriens interneurons. *Physiological Reports*, *9*, e14848. https://doi.org/10.14814/phy2.14848

Hirasawa, H., Contini, M., & Raviola, E. (2015). Extrasynaptic release of GABA and dopamine by retinal dopaminergic neurons. *Philosophical Transactions of the Royal Society of London. Series B, Biological Sciences*, *370*, 20140186. https://doi.org/10.1098/rstb.2014.0186

Hsia, A. Y., Vincent, J. D., & Lledo, P. M. (1999). Dopamine depresses synaptic inputs into the olfactory bulb. *Journal of Neurophysiology*, *82*, 1082–1085. https://doi.org/10.1152/jn.1999.82.2.1082

Huisman, E., Uylings, H. B. M., & Hoogland, P. V. (2004). A 100% increase of dopaminergic cells in the olfactory bulb may explain hyposmia in Parkinson's disease. *Movement Disorders*, *19*, 687–692. https://doi.org/10.1002/mds.10713

Kang, Y., & Kitai, S. T. (1993). A whole cell patch-clamp study on the pacemaker potential in dopaminergic neurons of rat substantia nigra compacta. *Neuroscience Research*, *18*, 209–221. https://doi.org/10.1016/0168-0102(93)90056-v

Khaliq, Z. M., & Bean, B. P. (2008). Dynamic, nonlinear feedback regulation of slow pacemaking by A-type potassium current in ventral tegmental area neurons. *The Journal of Neuroscience*, *28*, 10905–10917. https://doi.org/10.1523/JNEUROSCI.2237-08.2008

Khaliq, Z. M., & Bean, B. P. (2010). Pacemaking in dopaminergic ventral tegmental area neurons: Depolarizing drive from background and voltage-dependent sodium conductances. *The Journal of Neuroscience*, *30*, 7401–7413. https://doi.org/10.1523/JNEUROSCI.0143-10.2010

Kiyokage, E., Pan, Y.-Z., Shao, Z., Kobayashi, K., Szabo, G., Yanagawa, Y., Obata, K., Okano, H., Toida, K., Puche, A. C., & Shipley, M. T. (2010). Molecular identity of periglomerular and short axon cells. *The Journal of Neuroscience*, *30*, 1185–1196. https://doi.org/10.1523/JNEUROSCI.3497-09.2010

Korchynska, S., Rebernik, P., Pende, M., Boi, L., Alpár, A., Tasan, R., Becker, K., Balueva, K., Saghafi, S., Wulff, P., Horvath, T. L., Fisone, G., Dodt, H.-U., Hökfelt, T., Harkany, T., & Romanov, R. A. (2022). A hypothalamic dopamine locus for psychostimulant-induced hyperlocomotion in mice. *Nature Communications*, *13*, 5944. https://doi.org/10.1038/s41467-022-33584-3

Korshunov, K. S., Blakemore, L. J., Bertram, R., & Trombley, P. Q. (2020). Spiking and membrane properties of rat olfactory bulb dopamine neurons. *Frontiers in Cellular Neuroscience*, *14*, 60. https://doi.org/10.3389/fncel.2020.00060

Kosaka, T., Pignatelli, A., & Kosaka, K. (2020). Heterogeneity of tyrosine hydroxylase expressing neurons in the main olfactory bulb of the mouse. *Neuroscience Research*, *157*, 15–33. https://doi.org/10.1016/j.neures.2019.10.004

Lammel, S., Hetzel, A., Häckel, O., Jones, I., Liss, B., & Roeper, J. (2008). Unique properties of mesoprefrontal neurons within a dual mesocorticolimbic dopamine system. *Neuron*, *57*, 760–773. https://doi.org/10.1016/j.neuron.2008.01.022

Lammel, S., Steinberg, E. E., Földy, C., Wall, N. R., Beier, K., Luo, L., & Malenka, R. C. (2015). Diversity of transgenic mouse models for selective targeting of midbrain dopamine neurons. *Neuron*, *85*, 429–438. https://doi.org/10.1016/j.neuron.2014.12.036

Lüscher, C., Robbins, T. W., & Everitt, B. J. (2020). The transition to compulsion in addiction. *Nature Reviews. Neuroscience*, *21*, 247–263. https://doi.org/10.1038/s41583-020-0289-z

Ma, D., Herndon, N., Le, J. Q., Abruzzi, K. C., Zinn, K., & Rosbash, M. (2023). Neural connectivity molecules best identify the heterogeneous clock and dopaminergic cell types in the drosophila adult brain. *Science Advances*, *9*, eade8500. https://doi.org/10.1126/sciadv.ade8500

Margolis, E. B., Lock, H., Hjelmstad, G. O., & Fields, H. L. (2006). The ventral tegmental area revisited: Is there an electrophysiological marker for dopaminergic neurons? *The Journal of Physiology*, *577*, 907–924. https://doi.org/10.1113/jphysiol.2006.117069

McGann, J. P. (2013). Presynaptic inhibition of olfactory sensory neurons: New mechanisms and potential functions. *Chemical Senses*, *38*, 459–474. https://doi.org/10.1093/chemse/bjt018

McLean, D. L., & Fetcho, J. R. (2004). Ontogeny and innervation patterns of dopaminergic, noradrenergic, and serotonergic neurons in larval zebrafish. *Journal of Comparative Neurology*, *480*, 38–56. https://doi.org/10.1002/cne.20280

Montero, T., Gatica, R. I., Farassat, N., Meza, R., González-Cabrera, C., Roeper, J., & Henny, P. (2021). Dendritic architecture predicts in vivo firing pattern in mouse ventral tegmental area and substantia Nigra dopaminergic neurons. *Frontiers in Neural Circuits*, *15*, 769342. https://doi.org/10.3389/fncir.2021.769342

Morales, M., & Margolis, E. B. (2017). Ventral tegmental area: Cellular heterogeneity, connectivity and behaviour. *Nature Reviews. Neuroscience*, *18*, 73–85. https://doi.org/10.1038/nrn.2016.165

Morgan, J. L., Berger, D. R., Wetzel, A. W., & Lichtman, J. W. (2016). The fuzzy logic of network connectivity in mouse visual thalamus. *Cell*, *165*, 192–206. https://doi.org/10.1016/j.cell.2016.02.033

Neuhoff, H., Neu, A., Liss, B., & Roeper, J. (2002). I(h) channels contribute to the different functional properties of identified dopaminergic subpopulations in the midbrain. *The Journal of Neuroscience*, *22*, 1290–1302. https://doi.org/10.1523/JNEUROSCI.22-04-01290.2002

Otto, N., Pleijzier, M. W., Morgan, I. C., Edmondson-Stait, A. J., Heinz, K. J., Stark, I., Dempsey, G., Ito, M., Kapoor, I., Hsu, J., Schlegel, P. M., Bates, A. S., Feng, L., Costa, M., Ito, K., Bock, D. D., Rubin, G. M., Jefferis, G. S. X. E., & Waddell, S. (2020). Input connectivity reveals additional heterogeneity of dopaminergic reinforcement in drosophila. *Current Biology*, *30*, 3200–3211.e8. https://doi.org/10.1016/j.cub.2020.05.077

Papathanou, M., Dumas, S., Pettersson, H., Olson, L., & Wallén-Mackenzie, Å. (2019). Off-target effects in transgenic mice: Characterization of dopamine transporter (DAT)-Cre transgenic mouse lines exposes multiple non-dopaminergic neuronal clusters available for selective targeting within limbic Neurocircuitry. *eNeuro*, *6*, ENEURO.0198-19.2019. https://doi.org/10.1523/ENEURO.0198-19.2019

Pignatelli, A., Borin, M., Iseppe, A. F., Gambardella, C., & Belluzzi, O. (2013). The h-current in Periglomerular dopaminergic neurons of the mouse olfactory bulb. *PLoS ONE*, *8*, e56571. https://doi.org/10.1371/journal.pone.0056571

Pignatelli, A., Kobayashi, K., Okano, H., & Belluzzi, O. (2005). Functional properties of dopaminergic neurones in the mouse olfactory bulb: Dopaminergic neurones in the olfactory bulb. *The Journal of Physiology*, *564*, 501–514. https://doi.org/10.1113/jphysiol.2005.084632

Poewe, W., Seppi, K., Tanner, C. M., Halliday, G. M., Brundin, P., Volkmann, J., Schrag, A.-E., & Lang, A. E. (2017). Parkinson

disease. *Nature Reviews. Disease Primers*, *3*, 17013. https://doi.org/10.1038/nrdp.2017.13

Poulin, J.-F., Caronia, G., Hofer, C., Cui, Q., Helm, B., Ramakrishnan, C., Chan, C. S., Dombeck, D. A., Deisseroth, K., & Awatramani, R. (2018). Mapping projections of molecularly defined dopamine neuron subtypes using intersectional genetic approaches. *Nature Neuroscience*, *21*, 1260–1271. https://doi.org/10.1038/s41593-018-0203-4

Poulin, J.-F., Gaertner, Z., Moreno-Ramos, O. A., & Awatramani, R. (2020). Classification of midbrain dopamine neurons using single-cell gene expression profiling approaches. *Trends in Neurosciences*, *43*, 155–169. https://doi.org/10.1016/j.tins.2020.01.004

Pucak, M. L., & Grace, A. A. (1996). Effects of haloperidol on the activity and membrane physiology of substantia nigra dopamine neurons recorded in vitro. *Brain Research*, *713*, 44–52. https://doi.org/10.1016/0006-8993(95)01460-8

Puopolo, M., Raviola, E., & Bean, B. P. (2007). Roles of subthreshold calcium current and sodium current in spontaneous firing of mouse midbrain dopamine neurons. *The Journal of Neuroscience*, *27*, 645–656. https://doi.org/10.1523/JNEUROSCI.4341-06.2007

Roeper, J. (2013). Dissecting the diversity of midbrain dopamine neurons. *Trends in Neurosciences*, *36*, 336–342. https://doi.org/10.1016/j.tins.2013.03.003

Romanov, R. A., Zeisel, A., Bakker, J., Girach, F., Hellysaz, A., Tomer, R., Alpár, A., Mulder, J., Clotman, F., Keimpema, E., Hsueh, B., Crow, A. K., Martens, H., Schwindling, C., Calvigioni, D., Bains, J. S., Máté, Z., Szabó, G., Yanagawa, Y., … Harkany, T. (2017). Molecular interrogation of hypothalamic organization reveals distinct dopamine neuronal subtypes. *Nature Neuroscience*, *20*, 176–188. https://doi.org/10.1038/nn.4462

Schultz, W. (2016). Dopamine reward prediction error coding. *Dialogues in Clinical Neuroscience*, *18*, 23–32. https://doi.org/10.31887/DCNS.2016.18.1/wschultz

Sillitoe, R. V., & Vogel, M. W. (2008). Desire, disease, and the origins of the dopaminergic system. *Schizophrenia Bulletin*, *34*, 212–219. https://doi.org/10.1093/schbul/sbm170

Stuber, G. D., Stamatakis, A. M., & Kantak, P. A. (2015). Considerations when using cre-driver rodent lines for studying ventral tegmental area circuitry. *Neuron*, *85*, 439–445. https://doi.org/10.1016/j.neuron.2014.12.034

Tasic, B., Menon, V., Nguyen, T. N., Kim, T. K., Jarsky, T., Yao, Z., Levi, B., Gray, L. T., Sorensen, S. A., Dolbeare, T., Bertagnolli, D., Goldy, J., Shapovalova, N., Parry, S., Lee, C., Smith, K., Bernard, A., Madisen, L., Sunkin, S. M., … Zeng, H. (2016). Adult mouse cortical cell taxonomy revealed by single cell transcriptomics. *Nature Neuroscience*, *19*, 335–346. https://doi.org/10.1038/nn.4216

Tiklová, K., Björklund, Å. K., Lahti, L., Fiorenzano, A., Nolbrant, S., Gillberg, L., Volakakis, N., Yokota, C., Hilscher, M. M., Hauling, T., Holmström, F., Joodmardi, E., Nilsson, M., Parmar, M., & Perlmann, T. (2019). Single-cell RNA sequencing reveals midbrain dopamine neuron diversity emerging during mouse brain development. *Nature Communications*, *10*, 581. https://doi.org/10.1038/s41467-019-08453-1

Tufo, C., Poopalasundaram, S., Dorrego-Rivas, A., Ford, M. C., Graham, A., & Grubb, M. S. (2022). Development of the mammalian main olfactory bulb. *Development*, *149*, dev200210. https://doi.org/10.1242/dev.200210

Ungless, M. A., & Grace, A. A. (2012). Are you or aren't you? Challenges associated with physiologically identifying dopamine neurons. *Trends in Neurosciences*, *35*, 422–430. https://doi.org/10.1016/j.tins.2012.02.003

Vaaga, C. E., Borisovska, M., & Westbrook, G. L. (2014). Dual-transmitter neurons: Functional implications of co-release and co-transmission. *Current Opinion in Neurobiology*, *29*, 25–32. https://doi.org/10.1016/j.conb.2014.04.010

Wallace, M. L., & Sabatini, B. L. (2023). Synaptic and circuit functions of multitransmitter neurons in the mammalian brain. *Neuron*, *111*(19), 2969–2983. https://doi.org/10.1016/j.neuron.2023.06.003

White, R. B., & Thomas, M. G. (2012). Moving beyond tyrosine hydroxylase to define dopaminergic neurons for use in cell replacement therapies for Parkinson's disease. *CNS & Neurological Disorders Drug Targets*, *11*, 340–349. https://doi.org/10.2174/187152712800792758

Wolfart, J., Neuhoff, H., Franz, O., & Roeper, J. (2001). Differential expression of the small-conductance, calcium-activated potassium channel SK3 is critical for pacemaker control in dopaminergic midbrain neurons. *The Journal of Neuroscience*, *21*, 3443–3456. https://doi.org/10.1523/JNEUROSCI.21-10-03443.2001

Zhang, D.-Q., Zhou, T.-R., & McMahon, D. G. (2007). Functional heterogeneity of retinal dopaminergic neurons underlying their multiple roles in vision. *The Journal of Neuroscience*, *27*, 692–699. https://doi.org/10.1523/JNEUROSCI.4478-06.2007

How to cite this article: Lau, M. Y. H., Gadiwalla, S., Jones, S., & Galliano, E. (2024). Different electrophysiological profiles of genetically labelled dopaminergic neurons in the mouse midbrain and olfactory bulb. *European Journal of Neuroscience*, 1–20. https://doi.org/10.1111/ejn.16239